

## Estimating parameters of the nonlinear cloud and rain equation from a large-eddy simulation

Lunderman, Spencer; Morzfeld, Matthias; Glassmeier, Franziska; Feingold, Graham

**DOI**

[10.1016/j.physd.2020.132500](https://doi.org/10.1016/j.physd.2020.132500)

**Publication date**

2020

**Document Version**

Accepted author manuscript

**Published in**

Physica D: Nonlinear Phenomena

**Citation (APA)**

Lunderman, S., Morzfeld, M., Glassmeier, F., & Feingold, G. (2020). Estimating parameters of the nonlinear cloud and rain equation from a large-eddy simulation. *Physica D: Nonlinear Phenomena*, 410, Article 132500. <https://doi.org/10.1016/j.physd.2020.132500>

**Important note**

To cite this publication, please use the final published version (if applicable). Please check the document version above.

**Copyright**

Other than for strictly personal use, it is not permitted to download, forward or distribute the text or part of it, without the consent of the author(s) and/or copyright holder(s), unless the work is under an open content license such as Creative Commons.

**Takedown policy**

Please contact us and provide details if you believe this document breaches copyrights. We will remove access to the work immediately and investigate your claim.

# Estimating parameters of the nonlinear cloud and rain equation from a large-eddy simulation

Spencer Lunderman<sup>a</sup>, Matthias Morzfeld<sup>b</sup>, Franziska Glassmeier<sup>c,d,e</sup>, and Graham Feingold<sup>d</sup>

<sup>a</sup>Department of Mathematics, University of Arizona

<sup>b</sup>Institute of Geophysics and Planetary Physics, Scripps Institution of Oceanography,  
University of California, San Diego

<sup>c</sup>Department of Environmental Sciences, Wageningen University

<sup>d</sup>Chemical Sciences Laboratory/Earth System Research Laboratories, NOAA

<sup>e</sup>Currently at: Faculty of Civil Engineering and Geosciences Department of Geoscience and  
Remote Sensing, Delft University of Technology.

April 10, 2020

## Abstract

Predator-prey dynamics have been suggested as simplified models of stratocumulus clouds, with rain acting as a predator of the clouds. We describe a mathematical and computational framework for estimating the parameters of a simplified model from a large eddy simulation (LES). In our method, we extract cycles of cloud growth and decay from the LES and then search for parameters of the simplified model that lead to similar cycles. We implement our method via Markov chain Monte Carlo. Required error models are constructed based on variations of the LES cloud cycles. This computational framework allows us to test the robustness of our overall approach and various assumptions, which is essential for the simplified model to be useful. Our main conclusion is that it is indeed possible to calibrate a predator-prey model so that it becomes a reliable, robust, but simplified representation of selected aspects of a LES. In the future, such models may then be used as a quantitative tool for investigating important questions in cloud microphysics.

## Keywords

Predator-prey dynamics; Large-eddy simulation; Stratocumulus clouds; Bayesian inversion; Markov chain Monte Carlo;

## 1 Introduction

Stratocumulus cloud decks can reach 1000s of km in scale and cover vast stretches of the subtropical oceans. These decks consist of a space-filling arrangement of convective cells, with clouds marking updraft regions. Depending on the environmental conditions like sea-surface temperature or atmospheric aerosol, stratocumulus occur in two configurations (Agee, 1984; Wood and Hartmann, 2006; Glassmeier and Feingold, 2017)

- (i) wide updraft areas coinciding with cloud cells (“closed-cells”) whose *cloud-free boundaries* form a honeycomb-like pattern;
- (ii) narrow updrafts and cloudy rings that outline a honeycomb-like pattern (“open cells”).

37 Due to its lower cloud fraction, the open-cell configuration is significantly less reflective than the  
38 closed-cell configuration. Since roughly one fifth of the Earth’s surface is covered by stratocumulus  
39 cloud decks (Wood, 2012), the radiative effects of stratocumulus have a large impact on the Earth’s  
40 energy budget. In fact, stratocumulus remain one of the main sources of uncertainty in quantifying  
41 climate change (Boucher et al., 2013; Myhre et al., 2013; Schneider et al., 2017).

42 Stratocumulus, and in particular transitions from closed-cell to open-cell configurations, have  
43 been studied numerically with a hierarchy of mathematical and computational models. Large eddy  
44 simulations (LES) resolve the governing equations of moist hydrodynamics down to the cloud scale  
45 and can faithfully represent the formation of stratocumulus and how they transition between the  
46 open- and the closed-cell configurations, see, e.g., Feingold et al. (2015). In addition to these  
47 detailed but computationally expensive models, drastically simplified, low-dimensional models have  
48 been proposed to capture the spatial configuration of stratocumulus. For example, dynamic cellular  
49 networks can be used to describe the patterns that are formed within stratocumulus cloud systems  
50 (Glassmeier and Feingold, 2017). Predator-prey models, where the rain acts as the predator of  
51 clouds, have been proposed as phenomenological models for stratocumulus (Koren and Feingold,  
52 2011; Feingold and Koren, 2013; Koren et al., 2017).

53 The predator-prey models can reproduce two configurations that are relevant to stratocumulus  
54 clouds: oscillatory (limit cycle) and stationary solutions for cloud depth. The limit cycles model a  
55 scenario in which strong rain dissipates the cloud that created it, followed by renewed cloud build-up  
56 that proceeds until the cloud is again thick enough to produce strong rain, which restarts the whole  
57 process. A stationary cloud depth represents a situation in which the rain consumes the cloud at  
58 the same rate as the cloud replenishes.

59 We focus on one of the predator-prey models, the nonlinear cloud and rain equation of Koren  
60 et al. (2017), which we call KTF17 for short. Our primary goal is to build a mathematical and  
61 computational framework to convert KTF17 into a quantitative tool. We argue that this can be  
62 done by adopting a Bayesian approach, in which a posterior distribution over the parameters of  
63 KTF17 is defined based on cloud depth time series of stratocumulus. A natural data source for  
64 these time series would be observations of stratocumulus in the Earth’s atmosphere, e.g., derived  
65 from the Geostationary Operational Environmental Satellite-R Series (GOES-R). KTF17 does not  
66 account for horizontal advection which is usually present in satellite derived observations. Using  
67 observational data would thus require tracking stratocumulus patches within a larger cloud system  
68 over time to “remove” advection, see, e.g., Koren and Feingold (2013). To avoid these technicalities,  
69 we use LES output, generated in the absence of advection, as “data” in place of observations. The  
70 resulting KTF17 model, with stochastic parameters distributed according to a posterior distribution,  
71 is thus a quantitative, but simplified representation of selected aspects of cloud systems that are  
72 realistically represented by LES. Our approach thus connects the extreme ends of the hierarchy of  
73 cloud models and may be used to obtain new insights into complex cloud and rain interactions. Given  
74 the example of the predator-prey-based parameterization of Nuber and Graf (2005) to represent  
75 convection, simple predator-prey models, “calibrated” to a LES via a parameter estimation, may  
76 eventually even prove useful for representing some aspects of cloud systems in climate models. We  
77 focus, however, on establishing a suitable mathematical and computational framework for the task  
78 of “calibrating” a predator-prey model with LES data.

79 More specifically, we describe how parameters of KTF17 can be estimated from a LES by  
80 a “Bayesian inversion”. The inversion is based on two distributions: a prior distribution, that  
81 represents knowledge about the model parameters, *without* taking the data into account, and a  
82 likelihood, that describes the probability of the data, given a set of parameters, see, e.g., Reich  
83 and Cotter (2015); Asch et al. (2017); Tarantola (2005). Jointly, the prior and likelihood define  
84 a posterior distribution over the parameters that represents our knowledge of the parameters and

85 their uncertainties in view of the data, our prior knowledge and assumed errors.

86 Typically, a likelihood is based on a point-wise mismatch of model outputs and data. In our  
87 context, the “data” are a time series of cloud depth of the LES, i.e., a 2D field that evolves over  
88 time (note that we refer to simulation outputs as data because we treat them as such). KTF17,  
89 however, does not have an associated spatial scale. Thus, it is not straightforward to compare  
90 KTF17 to LES output. We address this issue by using “feature-based” likelihoods (Maclean et al.,  
91 2017; Morzfeld et al., 2018). The basic idea is that compressing the data into suitable features  
92 can bridge gaps between drastically simplified models and complex processes. The feature we  
93 consider is a stochastic representation of cycles of growth and decay in cloud depth, derived from  
94 the LES, that can be compared directly (point-wise) to limit cycles of KTF17. Required error  
95 models of the features are constructed based on variations of the cloud cycles extracted from the  
96 LES. We solve the resulting, feature-based inverse problem numerically by a Markov chain Monte  
97 Carlo (MCMC) method. This means that we generate a (large) set of physically relevant “samples”  
98 (model parameters) that lead to KTF17 limit cycles that are comparable to the cloud cycles observed  
99 in the LES, to within the assumed errors. In particular, we observe an overall good fit in terms of  
100 the cycle’s periods, amplitudes and average growth and decay times. The Bayesian approach and  
101 MCMC implementation further provide information about posterior errors and uncertainties, which  
102 in turn depend on expected model errors. This allows us to assess, in hindsight, the validity of our  
103 assumptions about errors and error models. We further carefully test the robustness of our overall  
104 approach by numerical sensitivity studies. These tests of robustness and of the validity of error  
105 models are essential to being able to use KTF17 to make precise and definite statements. Finally,  
106 we illustrate how to use our technique to investigate cloud microphysics questions. Specifically,  
107 we compute sensitivity of model parameters to temporal changes in the morphology of the cloud  
108 system. We must emphasize that our results and conclusions with respect to cloud microphysics  
109 are limited, in part because our study is limited to one particular LES.

## 110 **2 Background: the nonlinear cloud and rain equation, the LES and** 111 **feature-based Bayesian inversion**

112 We use a Bayesian approach to combine information from a LES with a simplified predator-prey  
113 model of stratocumulus clouds. In this section, we describe the predator-prey model and the LES.  
114 We then provide background and notation for Bayesian inversion and feature-based Bayesian inver-  
115 sion.

### 116 **2.1 The nonlinear cloud and rain equation (KTF17)**

117 The coevolution of cloud and rain can be captured, qualitatively, by predator-prey type dynamics  
118 and, more specifically, by differential equations with a delayed sink term (Koren and Feingold, 2011;  
119 Feingold and Koren, 2013; Koren et al., 2017). The delay stems from the fact that the predator  
120 (rain) is produced by the cloud (prey) with a delay that is associated with the time required for  
121 cloud droplets to coalesce to form larger raindrops. This delay time is a function of the amount of  
122 cloud water and the cloud drop concentration and is typically on the order of 15 minutes.

123 The predator-prey models are capable of reproducing two different dynamical regimes that are  
124 relevant to stratocumulus clouds. When the predator-prey models exhibit a constant cloud depth,  
125 the rain consumes the cloud at the same rate as cloud replenishment. When the predator-prey  
126 models exhibit oscillations (limit cycles), strong rain nearly depletes the cloud and then dissipates  
127 until the cloud is thick enough to again produce rain.

128 We consider the “nonlinear cloud and rain equation” (Koren et al., 2017), subsequently called  
 129 KTF17:

$$\frac{dH}{dt} = \frac{H_0 - H}{\tau} - \frac{\alpha}{\sqrt{N}} H^2 (t - T). \quad (1)$$

130 Here,  $H$  (in m) is cloud depth,  $H_0$  (in m) is the cloud depth carrying capacity,  $\tau$  (in days) is the  
 131 characteristic time to reach carrying capacity,  $T$  (in days) is the delay associated with the time  
 132 it takes to generate rain and  $N$  (in  $\text{cm}^{-3}$ ) is the droplet concentration; the scaling factor  $\alpha$  (in  
 133  $\text{day}^{-1}\text{m}^{-2.5}$ ) links the cloud depth, droplet concentration and rain rate (see Koren et al. (2017) for  
 134 further detail).

135 In summary, the parameters of the KTF17 model are the delay, the carrying capacity, the  
 136 characteristic time and the scaling factor. For a given set of parameters and initial conditions,  
 137 we solve (1) numerically by a 4th order Runge-Kutta method with time step  $\Delta t = 0.1$  min. The  
 138 numerical integration requires that we prescribe the cloud depth  $H(t)$  during “negative times” on  
 139 the interval  $t \in [-T, 0]$  and we assume that  $H(t)$  is constant during this interval. The result of a  
 140 numerical solution of KTF17 is a time series of cloud depth.

141 We note that KTF17 assumes that droplet concentration be fixed. This is justified when there  
 142 is an approximate balance between replenishment of aerosol particles, which form the nuclei for new  
 143 droplets, and consumption of droplets/particles via coalescence and their removal by rain. Below,  
 144 we use values between  $N = 16 \text{ cm}^{-3}$  and  $N = 45 \text{ cm}^{-3}$ , which are typical of the drop concentrations  
 145 in clean marine environments associated with open cellular convection and which are also in line  
 146 with the values of  $N$  in the LES we consider (see Section 2.2). Nonetheless, droplet concentration  
 147 may not be constant in a stratocumulus cloud system or in an LES ((Yamaguchi et al., 2017)). Thus,  
 148 the fixed droplet concentration may limit the usefulness of the KTF17 model in certain conditions.  
 149 We discuss these issues in more detail below.

## 150 2.2 Description of the LES

151 A LES is a detailed model of a cloud system in space (3D) and time. It solves the anelastic  
 152 Navier–Stokes equations on an Eulerian spatial grid, resolving convection and clouds, and in the  
 153 current work, also simulates microphysical processes such as the formation of droplets on suspended  
 154 particles (condensation nuclei), their growth by coalescence, and their removal by rain. We use the  
 155 LES output to estimate the parameters of KTF17, which produces a times series of cloud depth ( $H$   
 156 in (1)). During Bayesian inversion, we will connect KTF17 to the LES by extracting time series of  
 157 cloud depth from the LES (see Section 3.2).

158 We use the LES described in Feingold et al. (2015), with modifications. The atmospheric  
 159 conditions derive from a well studied drizzling stratocumulus case, but unlike Feingold et al. (2015),  
 160 the initial concentration of particles on which drops can form is about  $100 \text{ cm}^{-3}$  but decreases  
 161 naturally due to droplet coalescence and rain removal processes.

162 The spatial domain of the LES is 40 km by 40 km wide and 1.6 km high with a grid spacing  
 163 of 200 m in the horizontal and 10 m in the vertical. The simulation covers a total of 12 hrs with  
 164 a time step of one second. Simulation output is available every one minute. We disregard the first  
 165 4.5 hours of the LES during which the system rapidly transitions from a closed-cell to an open-cell  
 166 state. We thus only consider 7.5 hours, or 450 minutes, of simulation of an open-cell system for the  
 167 Bayesian inversion.

168 The KTF17 model describes cloud depth as a function of time, but not any other quantities  
 169 of the LES. For this reason, we consider cloud depth of the LES and disregard most other simu-  
 170 lation outputs with the exception of droplet concentration  $N$  and column liquid water path, (see

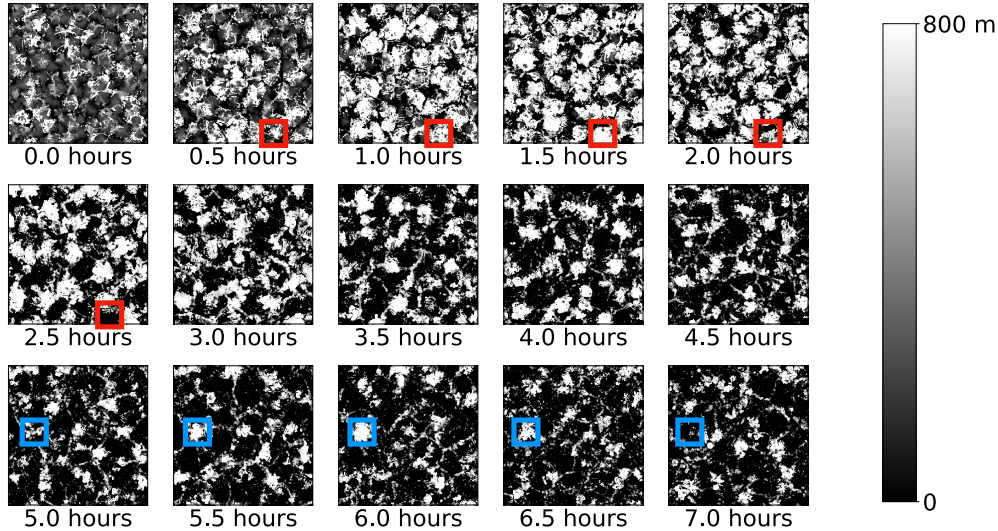


Figure 1: Snapshots, taken every 30 mins, of the 2D cloud depth field of the LES. Examples of cloud cycles, i.e., an increase in cloud depth, followed by a decrease in cloud depth, are highlighted by blue and red squares. After Feingold et al. (2015).

171 Section 3.2). Figure 1 shows snapshots of the cloud depth field over the span of 7 hrs, sampled  
 172 every 30 minutes, which is approximately the decorrelation timescale of the cloud field.

173 Figure 1 illustrates that, during the first 3.5 hrs, the system is characterized by a relatively dense  
 174 collection of clouds with high average cloud fraction; a gradual transition to a lower cloud fraction  
 175 then occurs as the cloud system self-organizes into a sparse collection of cloudy rings that outline  
 176 a honeycomb-like pattern of cloud-free cells. We will refer to the first 3.5 hrs of simulation as the  
 177 “dense phase” and to the remaining 4 hrs of simulation as the “sparse phase” (see Section 4.2). The  
 178 droplet concentration falls from about  $45 \text{ cm}^{-3}$  down to  $16 \text{ cm}^{-3}$  during the course of the 7.5 hrs  
 179 of simulation, as illustrated in Figure 2. We compute the droplet concentration over cloudy parts  
 180 of the domain by averaging  $N$  vertically and horizontally over the entire domain and scale this  
 181 average by the average cloud fraction. The consequences for parameter estimation with KTF17,  
 182 which assumes a constant  $N$ , will be discussed in detail below.

### 183 2.3 Bayesian inversion

184 Bayesian inversion means inferring information about model parameters from data. This is done  
 185 as follows. We denote the model parameters by the vector  $\boldsymbol{\theta}$  and we write the model as  $\mathcal{M}(\boldsymbol{\theta})$ .  
 186 The function  $\mathcal{M}$  could, for example, involve solving the KTF17 model numerically to produce time  
 187 series of cloud depth (see below). A priori, one may know a few things about the parameters. For  
 188 example, one may know that certain parameters must be positive to be physically relevant. In the  
 189 Bayesian framework, such “prior knowledge” is expressed as a prior distribution  $p_0(\boldsymbol{\theta})$ . Priors are  
 190 often uniform distributions. For example, if bounds on the parameters are known, then the prior  
 191 can be chosen uniformly within the bounds.

192 For a given  $\boldsymbol{\theta}$ , the numerical model can be simulated and its output can be compared to data,  
 193  $\mathbf{y}$ . Model and data are thus connected by

$$\mathbf{y} = \mathcal{M}(\boldsymbol{\theta}) + \boldsymbol{\eta}, \quad (2)$$

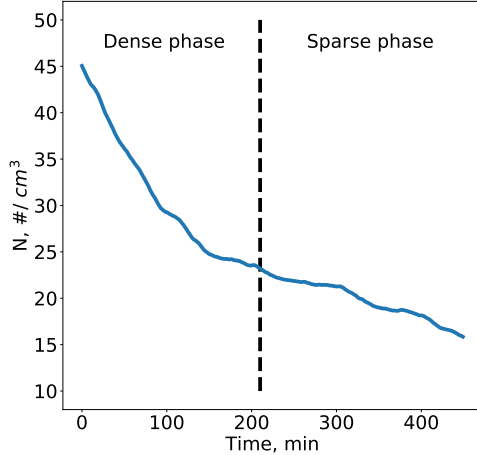


Figure 2: Droplet concentration  $N$ , scaled by average cloud cover, as a function of time. The dashed vertical line indicates the separation of the dense and sparse phases of the simulation

194 where  $\boldsymbol{\eta}$  represents discrepancies between the model and data, and is typically assumed to be  
 195 Gaussian distributed with mean zero and covariance matrix  $\mathbf{R}$ . Equation (2) then defines the  
 196 “likelihood”

$$p_l(\mathbf{y}|\boldsymbol{\theta}) \propto \exp\left(-\frac{1}{2}\|\mathbf{R}^{-1/2}(\mathbf{y} - \mathcal{M}(\boldsymbol{\theta}))\|^2\right), \quad (3)$$

197 where  $\mathbf{R}^{1/2}$  is a matrix square root and where the vertical bars denote the Euclidean norm. The  
 198 prior and likelihood jointly define the posterior distribution

$$p(\boldsymbol{\theta}|\mathbf{y}) \propto p_0(\boldsymbol{\theta}) p_l(\mathbf{y}|\boldsymbol{\theta}), \quad (4)$$

199 which describes our knowledge of the parameters and their uncertainties in view of the data. This  
 200 means, in particular, that a numerical model with parameters distributed according to the poste-  
 201 rior distribution, is “calibrated” to the data in the sense that simulations lead to model outputs  
 202 compatible with the data up to the assumed errors.

## 203 2.4 Feature-based Bayesian inversion

204 In many Bayesian inverse problems, the model  $\mathcal{M}$  is an accurate and detailed representation of  
 205 the physical process that generates that data. For example, atmospheric models used for “data  
 206 assimilation” and global numerical weather prediction, generate the full 3D atmospheric state. In  
 207 this case, Equation (2) directly connects model outputs to measurements of the atmospheric state  
 208 (data). This means that the likelihood (3) is a measure of the “point-wise” model-data mismatch,  
 209 e.g., describing the differences between the observations of the atmospheric states and the predictions  
 210 of the atmospheric model. Below, we will use Bayesian inversion to connect the outputs of a LES  
 211 with a very simple, phenomenological predator-prey model of stratocumulus clouds without an  
 212 associated spatial scale. The more common, point-wise definition of a likelihood is thus not useful  
 213 for our purposes and we use a “feature-based” approach. The idea is that while a simplified model  
 214 may not be able to reproduce the data in their entirety, it may be able to reproduce selected aspects  
 215 of the data, see Morzfeld et al. (2018). The selected aspects that *are* reproducible by the model  
 216 are called “features”. A feature-based inverse problem thus requires that we define features that are  
 217 comparable in the more usual “point-wise” sense.

218 Specifically, we define  $\mathcal{F}_{\mathcal{M}}(\boldsymbol{\theta})$  as a function that extracts the feature from the model and denote  
 219 by  $\mathbf{f}_y$  the feature extracted from the data. Assuming that discrepancies between the model feature  
 220 and the data feature can be accounted for by a random variable, we write

$$\mathbf{f}_y = \mathcal{F}_{\mathcal{M}}(\boldsymbol{\theta}) + \boldsymbol{\varepsilon}. \quad (5)$$

221 If  $\boldsymbol{\varepsilon}$  is Gaussian distributed with mean zero and covariance  $\mathbf{R}$  (with slight abuse of notation because  
 222  $\mathbf{R}$  was used above for another covariance matrix), the feature-based likelihood is

$$p_{l,f}(\mathbf{f}_y|\boldsymbol{\theta}) \propto \exp\left(-\frac{1}{2}\|\mathbf{R}^{-1/2}(\mathbf{f}_y - \mathcal{F}_{\mathcal{M}}(\boldsymbol{\theta}))\|^2\right). \quad (6)$$

223 We emphasize that the feature-based likelihood is defined by the Euclidian norm of the differences  
 224 of the model feature and the data feature. The feature-based likelihood measures the point-wise  
 225 mismatch of the features of model and data in the same way as the “usual” likelihood measures the  
 226 point-wise mismatch between the model outputs and the data (see above). Assuming that a prior  
 227  $p_0(\boldsymbol{\theta})$  for the model parameters is given, the feature-based posterior distribution is

$$p_f(\boldsymbol{\theta}|\mathbf{f}_y) \propto p_0(\boldsymbol{\theta}) \exp\left(-\frac{1}{2}\|\mathbf{R}^{-1/2}(\mathbf{f}_y - \mathcal{F}_{\mathcal{M}}(\boldsymbol{\theta}))\|^2\right). \quad (7)$$

228 In summary, a model with parameters distributed according to the feature-based posterior, produces  
 229 features that are compatible with the features extracted from the data, up to the assumed errors.  
 230 We emphasize that the prior has a direct influence on the shape of the posterior distribution, which  
 231 is just the product of prior and likelihood. Since parameter estimates are based on the posterior  
 232 distribution, a different choice of prior will ultimately result in different parameter estimates.

## 233 **2.5 Markov chain Monte Carlo for the numerical solution of Bayesian inverse** 234 **problems**

235 Monte Carlo methods can be used to numerically implement the (feature-based) Bayesian inversion.  
 236 The idea is to draw samples from the posterior distribution in such a way that averages over the  
 237 samples converge to expected values with respect to the posterior distribution when the number of  
 238 samples,  $N_e$  goes to infinity, see, e.g., Chorin and Hald (2013). In this sense, the samples, generated  
 239 by the Monte Carlo method, approximate the posterior distribution and can be used for inferences,  
 240 e.g., for computing the posterior mean and covariance matrix.

241 We use Markov chain Monte Carlo (MCMC) to draw posterior samples. A MCMC sampler  
 242 operates as follows. A sample is proposed by drawing from a proposal distribution and the proposed  
 243 sample is accepted with a probability that ensures that the stationary distribution of the Markov  
 244 chain is the targeted posterior distribution, see, e.g., Gilks et al. (1996). The various MCMC  
 245 samplers in the literature use different proposal mechanisms to speed up convergence, often by  
 246 exploring specific characteristics of the sampling problem. If one does not know of a particular  
 247 problem structure to exploit, one should use “general purpose” ensemble samplers, e.g., the affine  
 248 invariant MCMC ensemble sampler of Goodman and Weare (2010) or the t-walk of Christen et al.  
 249 (2010). These samplers are known to be effective for low-dimensional, nonlinear/non-Gaussian  
 250 problems and efficient implementations are also available.

251 To assess the accuracy of the MCMC solution one computes the integrated auto-correlation time  
 252 (IACT), see, e.g., Sokal (1996); Wolff (2004). The idea is that, while MCMC samples are generally  
 253 not independent, one can estimate an effective number of independent samples by

$$N_{s,\text{eff}} = \frac{N_s}{\text{IACT}}, \quad (8)$$



254 where  $N_s$  is the number of samples from the MCMC sampler. The reasoning is that if one has, e.g.,  
 255  $10^6$  samples, and one has computed IACTs of a few hundred, then one should expect an accuracy  
 256 that is comparable to that computed with thousands of independent samples.

### 257 3 Feature-based Bayesian inversion of the LES

258 The KTF17 model parameters are the carrying capacity  $H_0$ , the delay  $T$ , the characteristic time  
 259  $\tau$  and the scaling factor  $\alpha$ . We combine these four parameters in the parameter vector  $\boldsymbol{\theta} =$   
 260  $[H_0, \tau, T, \alpha]^T$ . Our goal is to compute the model parameters  $\boldsymbol{\theta}$  by a feature-based inversion of  
 261 the LES output. As described in Section 2.4, a feature-based inversion requires that we define a  
 262 prior distribution and a feature-based likelihood. We now describe in detail how these distributions  
 263 are constructed. The feature-based posterior follows from these two distributions and is used for  
 264 inferences, numerically implemented by MCMC.

#### 265 3.1 Prior distribution

266 The prior distribution describes our a priori knowledge of the KTF17 model parameters. We define  
 267 this prior to be a uniform distribution over the set of parameters that are (i) physically relevant  
 268 (positive); and (ii) lead to physically relevant limit cycles in KTF17. All parameters that satisfy  
 269 these conditions, receive the same nonzero prior probability while all other parameters receive  
 270 zero prior probability. Thus, a parameter vector  $\boldsymbol{\theta} = [H_0, \tau, T, \alpha]^T$  must satisfy the following four  
 271 conditions in order to receive non-zero prior probability.

- 272 1. All four model parameters must be positive.
- 273 2. The characteristic time to reach carrying capacity is longer than the delay time.
- 274 3. The parameter vector must produce solutions that are limit cycles.
- 275 4. Cloud depth must be positive.

276 For condition 3, we rely on the linear stability analysis in Koren et al. (2017). The parameters that  
 277 lead to limit cycles in KTF17 are characterized by the real part of a dimensionless parameter  $\beta$   
 278 being positive. Here,

$$\beta = \frac{\tau}{T} W \left( -2 \left[ \sqrt{\frac{1}{\mu} + \frac{1}{4}} - \frac{1}{2} \right] \frac{T}{\tau} \exp \left[ \frac{T}{\tau} \right] \right) - 1, \quad (9)$$

279 where  $\mu = \sqrt{N}/(\alpha\tau H_0)$  and  $W(\cdot)$  is the Lambert-W function. In other words, limit cycles occur  
 280 only if  $\text{Re}(\beta) > 0$ . Condition 4, i.e., checking for negative cloud depth, requires a simulation. For a  
 281 given  $\boldsymbol{\theta}$ , we solve KTF17 numerically and if we detect negative cloud depth, the parameter vector  
 282 receives zero prior probability. To streamline computations, we check for negative cloud depth after  
 283 checking conditions 1-3.

284 The prior is illustrated in terms of a “triangle plot” in the left panels of Figure 3. A triangle  
 285 plot contains histograms of all one and two-dimensional marginals of a given distribution, arranged  
 286 in the form of a triangle; each marginal is normalized so that the integral (area under the graph)  
 287 is equal to one. A triangle plot is, thus, a qualitative tool that illustrates regions in parameter  
 288 space that receive a large probability. Recall that the prior contains the information we have about  
 289 model parameters before the data are taken into account. Per our construction of the prior, this  
 290 means that a triangle plot of the prior illustrates regions in parameter space that lead to physically  
 291 relevant limit cycles of cloud depth.

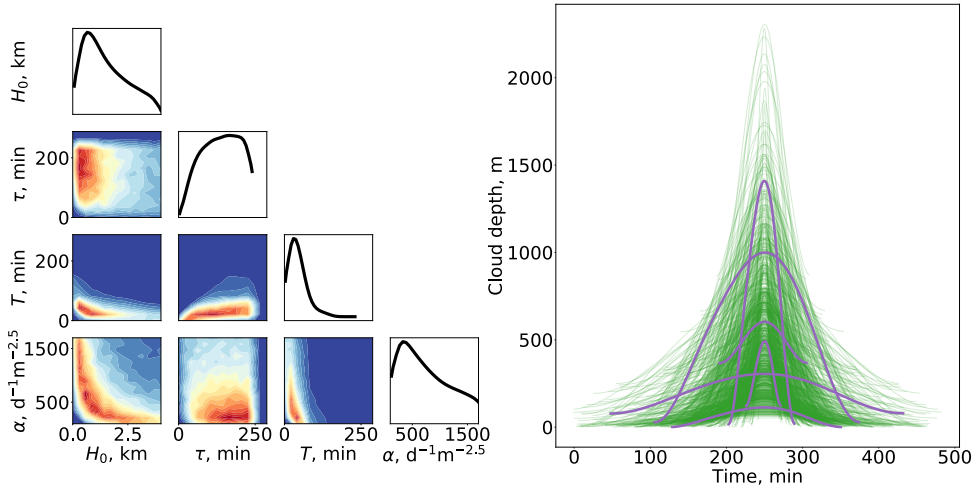


Figure 3: Left: Triangle plot of  $10^5$  samples of the prior distribution. Blue indicates a low probability while red indicates a high probability. Right:  $10^3$  limit cycles of KTF17 corresponding to  $10^3$  parameter vectors drawn at random from the prior. The cycles are aligned to reach their peak depths at the same time. Five examples of cloud cycles are highlighted in purple.

292 Generating the triangle plot requires that we draw samples from the prior which we do via  
 293 “importance sampling” with a proposal distribution that is uniformly distributed over the four-  
 dimensional hyper-cube defined by the lower and upper parameter bounds listed in Table 1 (for

	$H_0$ , m	$\tau$ , min	$T$ , min	$\alpha$ , $\text{days}^{-1}\text{m}^{-2.5}$
Lower bound	0	0	0	100
Upper bound	4000	288	288	2000
Prior mean	1650	137	43	836
Prior std. dev.	1067	61	27	495

Table 1: Mean and standard deviations computed from  $10^5$  samples of the prior.

294  
 295 more details about importance sampling, see, e.g., Owen (2013); Chorin and Hald (2013)). The  
 296 samples that constitute the triangle plot can also be used to compute prior means and standard  
 297 deviations, listed in Table 1. We note that the standard deviations are between 40%-60% of the  
 298 corresponding mean values, which indicates that the prior is “broad”, i.e., large parts of the parameter  
 299 space receive non-zero prior probability.

300 The “broadness” of the prior is further illustrated in the right panel of Figure 3, which shows one  
 301 period of  $10^3$  limit cycles of KTF17 corresponding to  $10^3$  prior samples of the prior (see Section 3.2  
 302 for details of how we compute these limit cycles). The limit cycles are arranged so that their maxima  
 303 occur at the same instant. We observe a large variance in the period and amplitude of the cloud  
 304 cycles. This means in particular that, a priori, we do not know the typical period or amplitude of a  
 305 cloud depth cycle. The goal of a Bayesian inversion is to refine the prior distribution to a posterior  
 306 distribution, which reduces variations in the cloud cycles via reducing variance in the parameters;  
 307 the reduction of variance of the parameters is achieved by taking the LES into account.

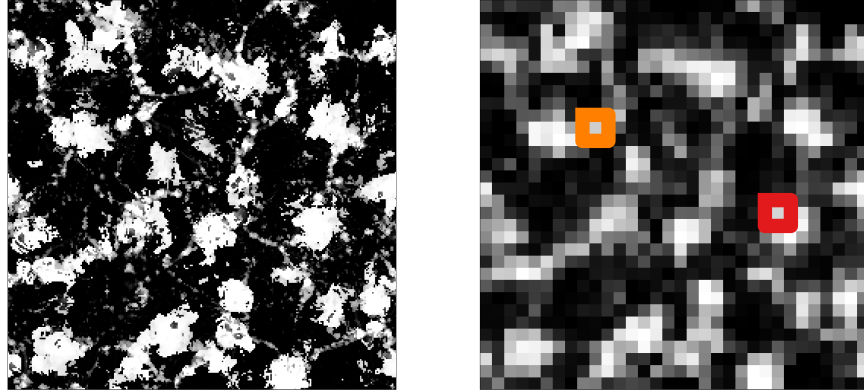


Figure 4: 2D cloud depth field at  $t = 4$  hrs at full resolution ( $256 \times 256$ , left) and spatially averaged cloud depth ( $32 \times 32$ , right). Time series of cloud depth for the locations encircled in red and orange are shown in Figure 5.

## 308 3.2 Feature-based likelihood

309 A feature-based likelihood requires that we define features of the model that can be compared  
 310 to features extracted from the data. We now describe how we construct these features and an  
 311 associated Gaussian error model.

### 312 3.2.1 Data feature

313 The data-feature is derived from the time varying 2D cloud depth field of the LES which defines  
 314  $256 \times 256$  time series of cloud depth at each grid point (with no advection present). These time  
 315 series, however, are noisy. To reduce the effects of this noise, we spatially average the 2D cloud depth  
 316 field over small, square “tiles” that contain a few grid points. We average cloud depth only over  
 317 regions where cloud exists, which we define by a positive integral of the liquid water content over the  
 318 depth of the cloud (liquid water path), taken from the LES. We considered several tile sizes for the  
 319 averaging and settled on tiles containing  $8 \times 8$  grid points (see also Section 4.1). With a horizontal  
 320 grid spacing of 200 m, this results in a “filter” length of about 1,600 m, which is large enough  
 321 to smooth out noise, but retains the main aspects of the cellular structure. The full resolution  
 322 ( $256 \times 256$ ) and the spatially averaged ( $32 \times 32$ ) cloud depth fields are illustrated in Figure 4.

323 The spatial averaging yields 1024 time series of cloud depth,  $H$ , over 7.5 hrs. We extract cycles  
 324 of growth and decay from these time series as follows. We first apply a temporal smoothing by  
 325 applying a Gaussian filter with a standard deviation of 10 minutes. We then compute local extrema  
 326 of the filtered time series via finite differencing. Two consecutive local minima define one cycle and  
 327 each cycle (without temporal smoothing) is stored. With this procedure, we extract 297 cycles from  
 328 the LES.

329 The procedure of the feature extraction is illustrated in Figure 5. Panels (a) and (b) show  $H$ ,  
 330 after temporal and spatial smoothing, at the locations encircled in red and orange in Figure 4.  
 331 Also shown are the extracted cycles (without temporal smoothing). The 297 cycles we compute are  
 332 shown in light blue in panel (c); the four cycles, shown in panels (a) and (b), are also shown (in  
 333 thicker purple, pink, brown and yellow lines). We align all cycles so that they reach their peaks at  
 334 the same instant and pad shorter cycles with zeros, so that all cycles have a duration of 270 minutes  
 335 (see also Section 4.1). The feature  $\mathbf{f}_y$  is the average of the 297 cycles, shown as a thick dark blue  
 336 line in panel (c).

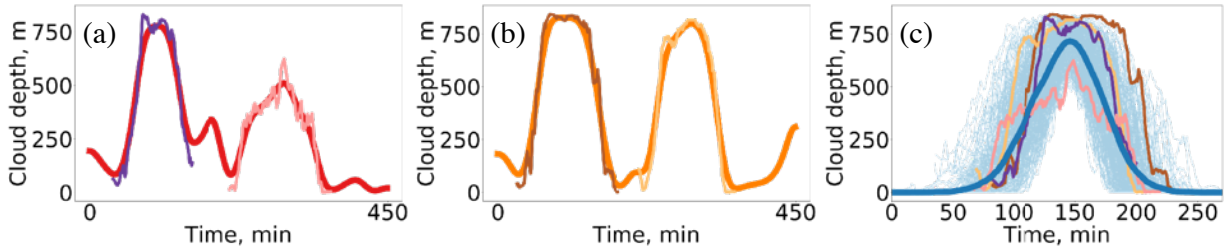


Figure 5: (a) Cloud depth time series after temporal smoothing (red) for the location encircled in red in the right panel of Figure 4. Shown in purple and pink are the two cycles extracted from this time series (without temporal smoothing). (b) Cloud depth time series after temporal smoothing (orange) for the location encircled in orange in the right panel of Figure 4. Shown in brown and yellow are the two cycles extracted from this time series (without temporal smoothing). (c) 297 cycles, extracted from the LES (without temporal smoothing), are shown in light blue. The cloud cycles from panels (a) and (b) are shown in a thicker purple, pink, brown and yellow lines. The dark blue line is the average of the 297 cycles.

### 3.2.2 Model feature

The model-feature is defined as one limit cycle of KTF17. The limit cycle and the time needed to reach it depend on the value of the model parameters and the initial condition. During the feature-based Bayesian inversion, implemented by an MCMC sampler (see below), the initial conditions are fixed, but we need to find limit cycles corresponding to different parameter values (all with non-zero prior probability).

To robustly compute limit cycles we use the following iterative scheme. We first solve KTF17 numerically for one day (the initial condition is  $H(t) = 0.1$  m for  $t \leq 0$ ) and approximate the time derivative of  $H(t)$  by finite differences to find the extrema of the cloud depth time series. The time instances of two consecutive local minima define one cycle of growth and decay (note that the data feature is defined in the same way). To check if a limit cycle is reached, we compare the root mean square error (RMSE) between the last two cycles and, if RMSE is less than 1 m, we stop the numerical solution and conclude that the system has reached its limit cycle. Otherwise, we continue the numerical solution of KTF17 for an additional day and, again, find local extrema to define cloud cycles and compute RMSE of the last two cycles. We repeat this process until two consecutive cycles are characterized by an RMSE of less than 1 m. The model-feature is then defined to be the last cycle of the cloud depth time series.

We align the peaks of the model- and data features and modify the model-feature to have the same duration (270 mins) as the data feature. Specifically, if the model feature has a shorter duration than the data feature, we pad the model feature with zeros (symmetrically before and after its peak). If the model feature is longer than the data feature, we truncate it (symmetrically before and after its peak).

Finally, we note that we are not aware of a proof that KTF17 has only *one* limit cycle for a given set of parameters with non-zero prior probability. Extensive numerical experiments, however, suggest that this is indeed the case. In particular, we performed a large number of simulations for several parameter vectors, drawn from the prior, starting at different initial conditions conditions  $0 < H(0) < 500$  m (with  $H(t) = H(0)$  for  $t < 0$ ) and, for each parameter vector, found only one limit cycle, independent of the initial conditions.

365 **3.2.3 Gaussian error model**

366 To finish the construction of the feature-based likelihood we need to define the errors  $\boldsymbol{\varepsilon}$  in Equa-  
 367 tion (5). As is customary, we assume a Gaussian distribution with a mean of zero. The covariance  
 368 matrix that defines the error model is computed based on the variations of the 297 cloud cycles  
 369 extracted from the LES. Specifically, we define the covariance  $\mathbf{P}$  as the sample covariance of the  
 370 297 cycles and then choose the covariance  $\mathbf{R}$  of  $\boldsymbol{\varepsilon}$  in (5) as

$$\mathbf{R} = \mathbf{P} + \sigma^2 \mathbf{I}, \quad (10)$$

371 where  $\mathbf{I}$  is the identity matrix and  $\sigma = 100$  m. Note that  $\mathbf{P}$ ,  $\mathbf{R}$  and  $\mathbf{I}$  are matrices of size  $270 \times 270$ ,  
 372 because each (padded) cloud cycle has a duration of 270 mins and the time step is one minute. We  
 373 use an additive “inflation” of the covariance  $\mathbf{P}$  because the padding leads to small variances at the  
 374 beginning and end of the 270 min time interval. We will assess, in hindsight, our assumptions about  
 375 errors in the features as well as how the padding with zeros affects the results in Section 4.

376 Each element of Equation (5) is now defined, which implies the feature-based likelihood by (6).  
 377 Together with the prior, the feature-based likelihood defines the feature-based posterior, which can  
 378 be written as

$$p_f(\boldsymbol{\theta}|\mathbf{f}_y) \propto \begin{cases} 0 & \text{if } p_0(\boldsymbol{\theta}) = 0, \\ \exp\left(-\frac{1}{2}\|\mathbf{R}^{-1/2}(\mathbf{f}_y - \mathcal{F}_{\mathcal{M}}(\boldsymbol{\theta}))\|^2\right) & \text{otherwise,} \end{cases} \quad (11)$$

379 where  $\mathbf{R}$ ,  $\mathbf{f}_y$  and  $\mathcal{F}_{\mathcal{M}}(\boldsymbol{\theta})$  are as above.

380 **3.3 Numerical solution by MCMC**

381 We use the python implementation of the t-walk (see <https://www.cimat.mx/jac/twalk/>) and the  
 382 python implementation “emcee” of the affine invariant ensemble sampler (Foreman-Mackey et al.,  
 383 2013). Below we only show results obtained by emcee, but results obtained by the t-walk are  
 384 qualitatively and quantitatively similar. The emcee sampler requires an ensemble of  $N_e$  “walkers”,  
 385 where

$$N_e \geq 2 \times (\text{number of model parameters}) = 8. \quad (12)$$

386 We chose an ensemble size of  $N_e = 20$ , because larger ensemble sizes are preferable (Foreman-  
 387 Mackey et al., 2013). The initial ensemble is generated as follows. We draw  $10^3$  samples from the  
 388 prior distribution and, for each one, evaluate (7), which is proportional to the posterior probability.  
 389 The 20 samples with the highest values, which also correspond to the samples with the highest  
 390 posterior probabilities, are the initial ensemble used in emcee.

391 Our code can be found at <https://github.com/SpenceLunderman/LMGF20> and can generate  
 392  $10^5$  samples in about 10 hrs and  $10^6$  samples in about 4 days (on a single core). For the results  
 393 shown below, we discard the first  $N_{\text{discard}}$  samples as “burn-in”, where  $N_{\text{discard}} = 5 \cdot \max \text{IACT}$ , and  
 394  $\max \text{IACT}$  is the largest IACT of the four parameters. Based on  $2 \cdot 10^6$  samples, we compute IACTs  
 395 of a few hundred (see below), which indicates that the number of samples we generate is sufficiently  
 396 large (accuracy comparable to thousands of independent samples).

397 **4 Results and discussion**

398 We perform the feature-based inversion, as described above, using a constant droplet concentration  
 399 of  $N = 25 \text{ cm}^{-3}$ , which is the time-average of  $N$  during the 7.5 hrs of simulation considered. In this  
 400 context, it is important to realize that the effect of a varying  $N$  over the range encountered in the  
 401 LES has a minor effect. The reason is that Equation (1) implies that changes in  $N$  result in a scaling

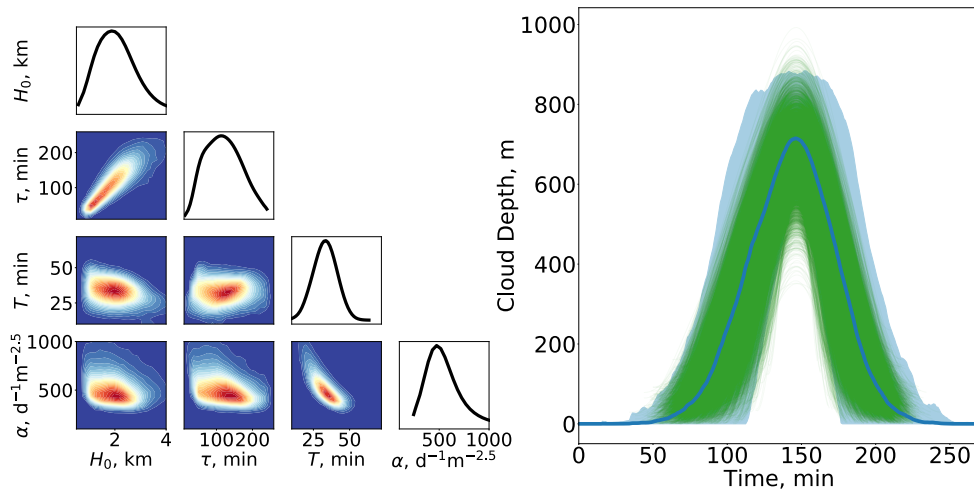


Figure 6: Left: Triangle plot of the posterior distribution ( $2 \cdot 10^6$  samples). Right: Shown in green are the limit cycles of KTF17 corresponding to  $10^4$  parameter vectors drawn at random from the posterior. The LES feature (average of 297 LES cloud cycles) is shown as a dark blue line. The light blue shaded region represents two sample standard deviations of the cloud cycles at each time instant (representing variations in the cloud cycles extracted from the LES).

402 of  $\alpha$  with the square root of  $N$ , but all other parameters are independent of the value of  $N$ . In  
 403 particular, if  $\alpha_0$  is estimated by assuming  $N = N_0$ , then setting  $N \rightarrow N_1$  results in  $\alpha_1 = \alpha \sqrt{N_1/N_0}$ .

404 The results of the feature-based inversion, based on an MCMC chain with  $2 \cdot 10^6$  samples, are  
 405 illustrated in Figure 6. The left panel shows a triangle plot of the posterior samples, obtained via  
 406 the MCMC, and the right panel shows  $10^4$  limit cycles of KTF17, corresponding to  $10^4$  parameter  
 407 vectors drawn at random from the posterior. Also shown are the LES feature and the variations in  
 408 the cloud cycles extracted from the LES. This figure should be compared to Figure 3, which shows  
 409 the same information *before* the Bayesian inversion, i.e., based on the prior distribution. We note  
 410 that the posterior distribution is more sharply peaked than the prior (note the different axes in the  
 411 triangle plots of Figures 3 and 6), which indicates that the LES derived feature indeed constrains  
 412 all four parameters of KTF17.

413 The sharpening of the prior to a feature-based posterior distribution can also be seen by com-  
 puting the sample mean and sample standard deviations, listed in Table 2. We note a shift in the

	$H_0$ , m		$\tau$ , min		$T$ , min		$\alpha$ , $\text{days}^{-1}\text{m}^{-2.5}$	
	Prior	Posterior	Prior	Posterior	Prior	Posterior	Prior	Posterior
Mean	1650	2063	137	120	43	33	836	548
Std.	1067	722	61	48	27	7	495	176
MAP	-	2062	-	131	-	36	-	450

Table 2: Mean and standard deviations of the prior and posterior distributions. The MAP of the posterior is also listed. Posterior quantities are computed from a MCMC chain with  $2 \cdot 10^6$  samples; prior quantities are computed from  $10^5$  samples of the prior.

414 sample mean and a reduction in sample standard deviations from the prior to posterior distribution.  
 415 Table 2 further lists the maximum a posteriori (MAP) estimates, i.e., the sample with the largest  
 416

417 posterior probability <sup>1</sup>. We note that the MAP and mean are not equal, which indicates that the  
 418 posterior distribution is not nearly Gaussian. In this context, it is also important to realize that the  
 419 posterior mean is *not* a posterior sample, i.e., its posterior probability can be zero (because it may  
 420 not satisfy all four prior constraints). For this reason, the MAP may be a more useful estimate of  
 421 the KTF17 parameters than the posterior mean.

422 The left panel of Figure 6 illustrates that cycles of KTF17, obtained by numerical solution of  
 423 KTF17 with parameters sampled from the posterior, are well within the variations of the cloud  
 424 cycles extracted from the LES. This indicates that our error model and the error covariance matrix  
 425  $\mathbf{R}$  are reasonable. Here, we tuned, to some extent, the additive inflation defined by  $\sigma$  in (10). Recall  
 426 that error models are notoriously difficult to come by because error models represent “what we do  
 427 not know” about the system. Our approach here is to introduce a tunable covariance inflation factor,  
 428  $\sigma$ , that is selected so that the posterior uncertainties, as illustrated by the trajectory ensemble in  
 429 the right panel of Figure 6, are reasonable, and within the expected uncertainties, derived directly  
 430 from the LES.

431 We can use the results of the feature-based inversion to investigate if the cycles of KTF17 have  
 432 similar properties as the cycles extracted from the LES. Specifically, we can consider the period,  
 433 amplitude, and growth and decay times of the KTF17 and LES derived cycles. Here, the period  
 434 is the duration of the cloud cycle (without zero padding); the amplitude is the difference between  
 435 the maximum and minimum cloud depth reached during a cycle <sup>2</sup>. The cycle growth time describes  
 436 how long it takes a cloud to build up to its maximum cloud depth, and the decay time describes  
 437 how long it takes to decay from maximum cloud depth to its minimum (equivalently, the decay time  
 438 is equal to the period minus the growth time). These four properties are computed for each cloud  
 439 cycle extracted from the LES and for  $10^4$  KTF17 limit cycles, defined by parameters that are drawn  
 440 from the posterior distribution. The means and standard deviations of the four cycle properties  
 are listed in Table 3. We note that the mean of each cycle property, computed from KTF17, is

	Period, min		Amplitude, m		Growth time, min		Decay time, min	
	LES	KTF17	LES	KTF17	LES	KTF17	LES	KTF17
Mean	137	119	619	591	69	66	69	55
Std. Dev.	23	26	142	102	23	15	19	12

Table 3: Mean and standard deviations of cloud cycle properties of the LES and KTF17. LES results are computed from 297 cycles and KTF17 results are computed from  $10^4$  simulations with parameters drawn from the posterior distribution.

441 within one standard deviation of the mean of the corresponding property computed from the LES.  
 442 Moreover, the standard deviations of the LES and KTF17 cycle properties are also comparable,  
 443 which suggests an overall good “fit” of KTF17 to the LES in terms of these cycle properties.  
 444

445 To report on the statistical accuracy of the MCMC solution, we list the IACTs, estimated from  
 446 the  $2 \cdot 10^6$  samples, of all four parameters in Table 4. The IACTs are less than  $10^3$ , which indicates  
 447 that the number of samples is sufficient to accurately compute posterior means, standard deviations

<sup>1</sup>It is important to remember that marginal distributions, shown in the form of histograms in the triangle plots, are not “projections” of the multivariate probability distribution. For this reason, the maxima of the posterior marginals (histograms) do not correspond to the mode of the multivariate posterior distribution (MAP).

<sup>2</sup>We emphasize that the blue line, shown in Figure 6, is the average of the LES cycles, but taking into account the zero padding, and stitching the cloud cycles together at their maximum value. This means that the maximum value of the blue line in Figure 6 equals the average maximum cloud depth over all cycles, which is different from the average amplitude in Table 3. The same reasoning explains why the average amplitude of KTF17, reported in Table 3, is different from what one might expect by visually taking the average of the green lines in Figure 6.

$H_0$ , m	$\tau$ , min	$T$ , min	$\alpha$ , days <sup>-1</sup> m <sup>-2.5</sup>
620	326	539	665

Table 4: Integrated autocorrelation times (computed from the  $2 \cdot 10^6$  samples).

448 and the MAP, with an effective sample size in the thousands.

#### 449 4.1 Robustness of the LES feature

450 The computational framework we describe, and in particular the construction of the LES feature,  
451 relies on several assumptions and modeling choices. The Bayesian approach and MCMC implemen-  
452 tation allow us to investigate, numerically, the validity of our assumptions and choices. We already  
453 described the effects of the error model and our choice of additive covariance inflation (see Figure 6).  
454 We now investigate the robustness of the LES feature to two other modeling choices: the spatial  
455 smoothing and the zero-padding of the cloud cycles (see Section 3.2.1).

##### 456 4.1.1 Robustness to spatial smoothing

457 While it is difficult to determine the precise amount of spatial smoothing, it is clear that (i) smooth-  
458 ing is necessary, or else the cloud depth time series are too noisy; and (ii) that there is a maximum  
459 amount of smoothing that should not be exceeded, or else the effects of cloud entities are averaged  
460 out. We investigate this issue by performing the feature-based Bayesian inversion for three spatial  
461 averages over “tiles” consisting of  $4 \times 4$ ,  $8 \times 8$  and  $16 \times 16$  grid points respectively. With each spatial  
462 averaging, we compute the data-feature and perform the Bayesian inversion via MCMC, generating  
463  $2 \cdot 10^6$  samples in each configuration. In all three cases, the prior distribution is the same as above,  
464 because the prior is independent of the definition of features, or, equivalently, the likelihood. We also  
465 keep all other aspects (covariance inflation, temporal smoothing etc.), that define the data-feature,  
466 as above.

467 Table 5 lists the posterior mean, standard deviation and MAP estimates for three spatial smooth-  
ings, computed from three MCMC runs with  $2 \cdot 10^6$  samples. We note that the parameter estimates

Tile width	$H_0$ , m			$\tau$ , min			$T$ , min			$\alpha$ , days <sup>-1</sup> m <sup>-2.5</sup>		
	4	8	16	4	8	16	4	8	16	4	8	16
Mean	2344	2063	1776	114	120	141	29	33	41	560	548	458
Std.	989	722	544	48	48	49	7	7	6	183	176	83
MAP	2147	2062	2215	119	131	188	34	36	42	453	450	414

Table 5: Posterior means, standard deviations, and MAP estimates for the four parameters of KTF17 and for the three configurations which differ in their spatial smoothing of the LES cloud depth field. Posterior means, the MAP, and standard deviations are computed from the MCMC chain with  $2 \cdot 10^6$  samples.

468 for the three configurations are within a standard deviation of each other, independently of which  
469 standard deviation one choses to use. The only exception is the parameter  $T$ , where the estimates  
470 for the  $16 \times 16$  case are within two standard deviations of the  $4 \times 4$  or  $8 \times 8$  scenario. A smoothing  
471 over  $16 \times 16$  grid points may, therefore, be labeled as excessive.  
472

473 Nonetheless, averaging over tiles of size  $4 \times 4$  or  $8 \times 8$  gives nearly identical results, which indicates  
474 some robustness of our approach with respect to spatial smoothing. We emphasize, however, that



475 a significantly larger amount of smoothing (tiles consisting of more than  $16 \times 16$  grid points) does  
 476 not lead to reasonable parameter estimates because the effects of cloud entities are averaged out.

### 477 4.1.2 Robustness to padding of LES cycles

478 In the construction of the LES feature, cycles are aligned at their peaks of cloud depth. The cycles  
 479 are then “padded with zeros” so that all cycles have the same duration (270 min). The LES feature  
 480 is simply the average of the padded cycles. Below, we call this construction “Version (a)”. We now  
 481 investigate the consistency of the parameter estimation results when we choose another method to  
 482 derive the LES feature that does not make use of zero padding.

483 In “Version (b)”, we again align all cloud cycles at their peaks, but rather than padding with  
 484 zeros, we average only those cycles that “exist”, i.e., which have non-zero cloud depth at a given time  
 485 instant. We further exclude all instances where less than 10 cycles exist. The error covariance of  $\epsilon$   
 486 for Version (b) is computed in the same way as in Version (a). Figure 7 illustrates the LES feature of  
 487 versions (a) and (b). Note that the duration of the average in Version (b) is shorter than in Version  
 488 (a) because we only consider instances when at least 10 cycles are non-zero and longer cycles occur  
 489 less frequently. We further note that near the peak, these two versions are equal because, at peak  
 490 times, zero padding in Version (a) has no effect and no cycles are excluded in Version (b) because  
 491 more than 10 cycles exist.

492 We perform a feature-based Bayesian inversion for LES features constructed using versions (a)  
 and (b) and, as before, generate  $2 \cdot 10^6$  samples by MCMC. Results are shown in Table 6.

	$H_0$ , m		$\tau$ , min		$T$ , min		$\alpha$ , days <sup>-1</sup> m <sup>-2.5</sup>	
	Version (a)	Version (b)	V. (a)	V. (b)	V. (a)	V. (b)	V. (a)	V. (b)
Mean	2063	2008	120	126	33	35	548	526
Std.	722	684	48	50	7	9	176	180
MAP	2062	2321	131	164	36	38	450	430

Table 6: Posterior means, standard deviations and MAP estimates for the four parameters of KTF17 and for the two configurations which differ in their calculation of the LES feature. Version (a) and Version (b) correspond to the two LES features shown in Figure 7. Posterior means, the MAP and standard deviations are computed from the MCMC chain with  $2 \cdot 10^6$  samples.

493 We note that the parameter estimates resulting from versions (a) and (b) are not significantly  
 494 different. The reason is that most KTF17 cycles occur between 50 and 200 minutes (see Figure 6),  
 495 i.e., when the two LES features of versions (a) and (b) are similar. The similarities between these  
 496 two posterior distributions can also be seen in the marginal distributions in Figure 8. The left panel  
 497 shows a triangle plot of the posterior distribution of Version (a) and the left panel shows a triangle  
 498 plot of the posterior distribution of Version (b). In both panels, the plots on the diagonals show the  
 499 one-dimensional marginal distributions of both posteriors in black (Version (a)) and blue (Version  
 500 (b)). In summary, the similarity in the parameter estimates and posterior distributions of Versions  
 501 (a) and (b) suggests that estimation framework we describe is robust to small changes in the details  
 502 of how one calculates the data feature.  
 503

## 504 4.2 Studying changes in cloud system morphology

505 The Bayesian inversion and the KTF17 model will prove useful if one can map meteorological  
 506 conditions to changes in the parameters of KTF17. We illustrate how to do this with a simple  
 507 example in which we start to investigate the effects of large-scale changes within the cloud field on

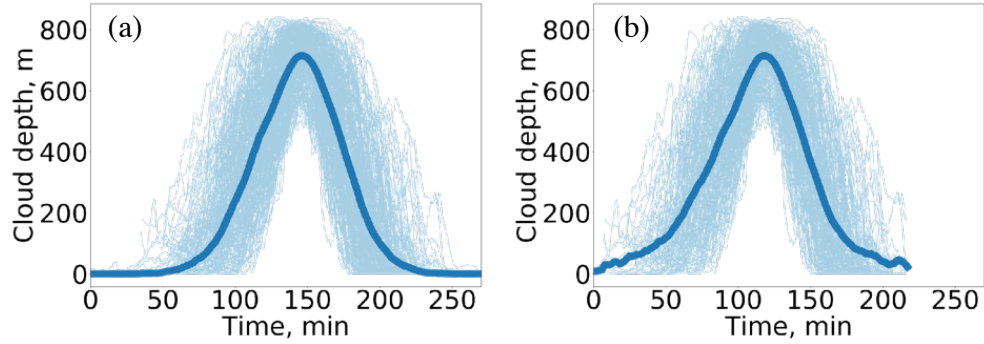


Figure 7: Cloud cycles and data feature of Version (a) (left) and Version (b) (right). Light blue: LES cycles. Thick blue: LES feature.

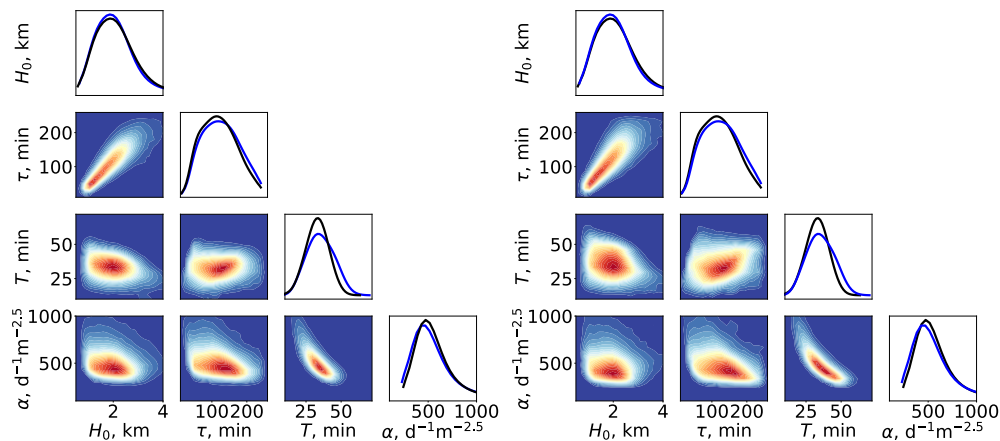


Figure 8: Left: triangle plot of the posterior distribution of Version (a). Right: triangle plot of the posterior distribution of Version (b). The diagonal plots of each panel show the one-dimensional marginals of both distributions (in black for Version (a), in blue for Version (b)). All plots are based on  $2 \cdot 10^6$  MCMC samples.

508 the parameters of KTF17. We base this investigation on only one LES, which represents one cloud  
 509 system and, for that reason, our results and conclusion are limited.

510 We note that the cloud system undergoes a change in its morphology from a relatively dense  
 511 cloud configuration with a higher average cloud fraction to a sparse coverage with a lower average  
 512 cloud fraction (see Figure 1). During this transition, the droplet concentration also decreases (see  
 513 Figure 2). The transition occurs roughly at the 3.5 hour mark and aligns with a change in the  
 514 thickness of the boundary layer, whose thickness increases until about 3.5 hours, and then decreases.

515 To investigate the effects of the morphological change in the macro-structure of the cloud system  
 516 on the parameters of KTF17, we perform two feature-based inversions as follows. We separate  
 517 the cloud cycles, extracted from the LES, into two groups: cycles occurring before and after the  
 518 transition from the dense to the sparse cloud cover, i.e., before or after 3.5 hr. For example, the  
 519 cloud cycles shown in purple and brown in panels (a) and (b) of Figure 5 occur before the transition  
 520 (dense phase), but the cycles shown in pink and yellow occur after the transition (sparse phase).  
 521 In this way, we obtain 166 cycles during the dense phase and 131 during the sparse phase, shown  
 522 along with their averages (using zero-padding) in Figure 9.

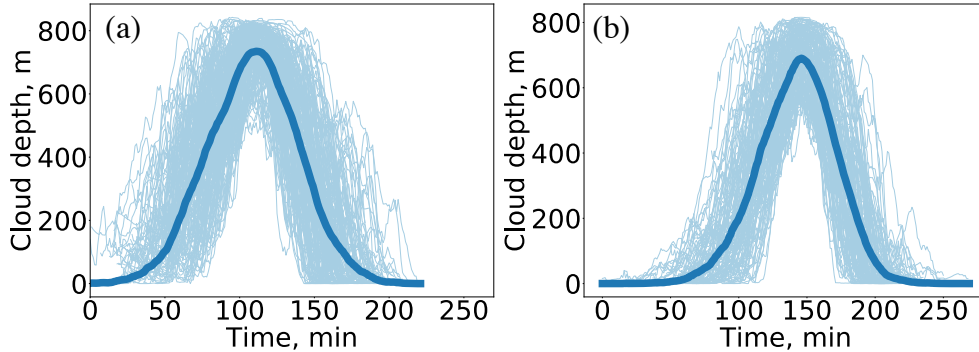


Figure 9: Cloud cycles and data feature for the dense (a) and sparse phases (b). Light blue: LES cycles. Thick blue: LES feature.

523 We compute data-features separately for the dense and sparse phases using the techniques  
 524 described above (using the default spatial smoothing over tiles consisting of  $8 \times 8$  grid points and  
 525 Version (a), i.e., zero padding of the cycles). In this way, we define feature-based likelihoods for  
 526 the dense and sparse phases. We use the same prior for the dense and sparse phases to define  
 527 two posterior distributions. We assign the time average of the droplet concentration in Figure 2,  
 528 computed separately over the dense and sparse phases, as the values used for  $N$  in the Bayesian  
 529 inversion. Specifically, we chose  $N = 31 \text{ cm}^{-3}$  for the dense phase and  $N = 20 \text{ cm}^{-3}$  for the sparse  
 530 phase. As before, we use the MCMC sampler to draw  $2 \cdot 10^6$  samples from the posterior distributions  
 531 associated with the dense and sparse phases.

Table 7 lists parameter estimation results for the two dense and sparse phases. We note that

	$H_0$ , m		$\tau$ , min		$T$ , min		$\alpha$ , $\text{days}^{-1}\text{m}^{-2.5}$	
	Dense	Sparse	Dense	Sparse	Dense	Sparse	Dense	Sparse
Mean.	2028	1886	122	110	36	32	525	535
Std.	615	616	45	44	6	7	117	166
MAP	2112	2408	130	165	36	36	483	405

Table 7: Maximum a posteriori (MAP) estimate, posterior mean and posterior standard deviation for the dense and sparse phases, computed from MCMC chains with  $2 \cdot 10^6$  samples.

532 the parameter estimates (posterior mean and MAP) are within one standard deviation of each  
 533 other. Furthermore, the parameter estimates listed in Table 7 are comparable with the parameters  
 534 in Table 5, which are estimated based on *all* cloud cycles extracted from the LES (i.e., cycles in  
 535 dense and sparse configurations). Similarities and differences in the parameter estimates can also  
 536 be illustrated by triangle plots of the two posterior distributions, shown in Figure 10. The left panel  
 537 shows the posterior distribution associated with the dense phase; the right panel shows the posterior  
 538 distribution associated with the sparse phase. It is apparent that the posterior distributions are  
 539 quite similar, but it is also apparent that there are differences, especially in the delay  $T$  and the  
 540 scaling factor  $\alpha$ .  
 541

542 It is difficult to determine whether or not the differences in the parameter estimates are sig-  
 543 nificant. Taking into account the standard deviations as an indicator of uncertainty, one may be  
 544 tempted to conclude that the differences are not significant. One can study this further by compar-  
 545 ing the differences in parameter estimates induced by the dense and sparse phases, with differences  
 546 induced by variations in the smoothing or paddings. Figure 11 illustrates this point and shows 1D

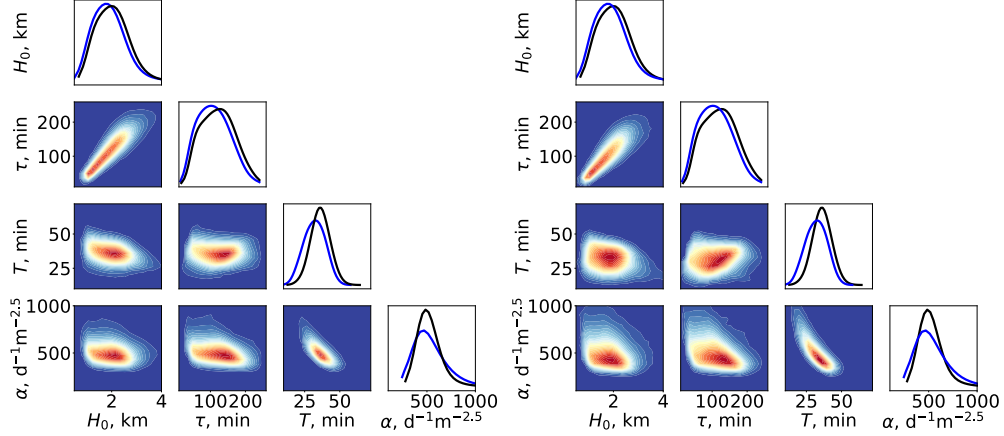


Figure 10: Left: triangle plot of the posterior distribution associated with the dense phase. Right: triangle plot of the posterior distribution associated with the sparse phase. The diagonal plots of each panel show the one-dimensional marginals of both distributions (in black for the dense, in blue for the sparse phase). All plots are based on  $2 \cdot 10^6$  MCMC samples.

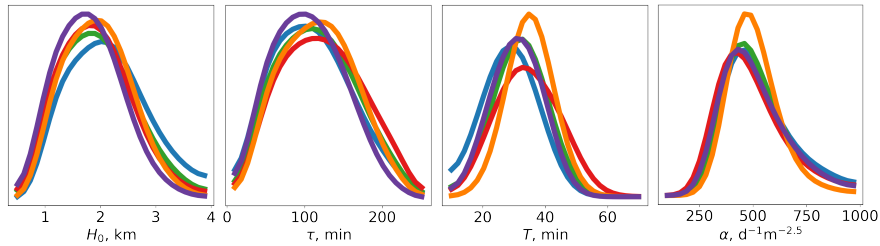


Figure 11: Marginal posterior distributions over the four parameters. Left to right:  $H_0$ ,  $\tau$ ,  $T$  and  $\alpha$ . Green:  $8 \times 8$  spatial smoothing, zero padding, all cycles. Blue:  $4 \times 4$  spatial smoothing, zero padding, all cycles. Red:  $8 \times 8$  spatial smoothing, no padding, all cycles. Orange:  $8 \times 8$  spatial smoothing, zero padding, dense cycles. Purple:  $8 \times 8$  spatial smoothing, zero padding, sparse cycles.

547 posterior marginals over the four parameters for five of the cases considered. Three of the cases  
 548 (green, blue and red in Figure 11) indicate uncertainty in parameter estimates induced by variations  
 549 in the numerical setup. Variation in the posterior distributions indicates the variability one should  
 550 expect due to different choices in the numerics. We then overlay the posterior distributions defined  
 551 by only the dense or only the sparse phase cycles (orange and purple in Figure 11). The variation of  
 552 these distributions indicates variability in the parameter estimates caused by changes in the large  
 553 scale structure of the cloud system. We note, as before, the largest differences in the delay  $T$  and  
 554 the scaling factor  $\alpha$ .

555 One can further investigate how differences in the parameter estimates propagate to character-  
 556 istics of the cloud cycles, such as their period, amplitude, and growth and decay times (see above  
 557 for definitions). We compute the period, amplitude, and growth and decay times based on the LES  
 558 for three cases (i) using all cycles; (ii) using only cycles of the dense phase; (iii) using only cycles  
 559 of the sparse phase. We then repeat this procedure for the KTF17 model with parameters drawn  
 560 from the posterior distributions corresponding to the above three cases. Figure 12 illustrates this  
 561 point. Here we plot the average and standard deviation of the cloud cycle properties for the LES  
 562 (left) and KTF17 (right) for the three cases; all quantities are scaled by the associated mean value

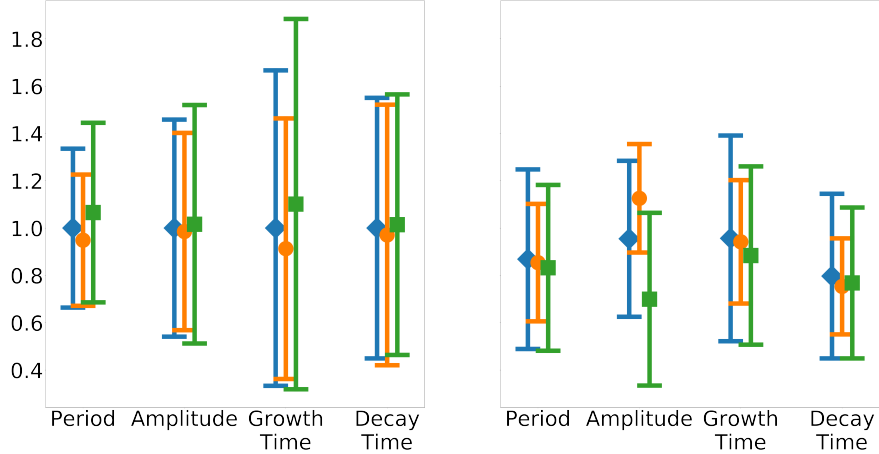


Figure 12: Mean and standard deviation of the period, amplitude, growth time and decay time of cloud cycles. Left: LES. Right: KTF17. Blue diamond – all cycles. Orange circle – dense cycles. Green square – sparse cycles. All quantities are scaled by the average values computed from all cycles of the LES.

563 of the LES case (i). We note that the properties of the LES do not change dramatically when  
 564 moving from dense to sparse phases. Moreover, the cycle properties of KTF17 are comparable with  
 565 those of the LES, but we observe a larger spread in the amplitude. Since the cycle properties do  
 566 not change much during the transition from the dense to the sparse phase, one might expect that  
 567 parameters of the KTF17 model should also be largely unaffected by this transition. Taking also the  
 568 similarities in the parameter estimates and posterior distributions into account, one might conclude  
 569 that the cycles of cloud patches within a cloud system may not necessarily be affected by changes  
 570 in the macro-structure of the cloud system. This conclusion, however, is based on a single LES,  
 571 which represents a case study with specific large-scale and thermodynamic boundary conditions. It  
 572 is conceivable that KTF17 parameters will be sensitive to these boundary conditions.

## 573 5 Summary and conclusions

574 Stratocumulus clouds are an important part of the Earth system and have a large effect on Earth’s  
 575 overall radiative balance and climate. For these reasons, stratocumulus cloud systems are studied  
 576 computationally by a hierarchy of models ranging from simplified, phenomenological models to cloud  
 577 resolving simulations of the atmosphere. We described a conceptual and computational strategy  
 578 for turning a simplified, phenomenological model into a quantitative tool. Specifically, we use the  
 579 nonlinear rain equation (KTF17) and estimate its parameters from the outputs of a large eddy  
 580 simulation (LES).

581 The main technical difficulty for such a parameter estimation is that the phenomenological model  
 582 and the LES operate in vastly different regimes in terms of what the two models are actually capable  
 583 of. In particular, the LES has temporal and spatial scales, whereas KTF17 has no associated spatial  
 584 scale. We overcame these difficulties by realizing that the KTF17 model produces cycles of cloud  
 585 growth and decay that are comparable to cycles within the LES. We use cycles of growth and decay  
 586 to define “features” and base the parameter estimation on these features. This includes deriving  
 587 error models for the features which in turn allows us to formulate the parameter estimation problem  
 588 within the Bayesian framework. The resulting Bayesian inverse problem is solved numerically by a

589 Markov chain Monte Carlo method, which allows us to assess posterior uncertainties.

590 We carefully studied the validity of our assumptions and modeling choices. The error model,  
591 which is notoriously difficult to construct because it represents “what we do not know”, was set up to  
592 have one tunable parameter (defining an additive covariance inflation). This parameter is tuned so  
593 that posterior uncertainties are reasonable and match the variability in the cycles derived from the  
594 LES. In addition, we investigated the robustness of our approach to the details of the construction  
595 of the features (spatial smoothing of the LES cloud depth fields and zero-padding of resulting  
596 cloud cycles). Stringent tests of this type are necessary to show that the estimated parameters are  
597 precise enough for drawing conclusions. Our numerical experiments indeed suggest that the KTF17  
598 model, with parameters distributed according to the feature-based posterior distribution, is robustly  
599 capable of representing cloud cycle properties of a LES.

600 As an illustration of how one may use a simplified model as a quantitative tool, we investigated  
601 the sensitivity of the KTF17 parameters to morphological changes within the cloud system simulated  
602 by the LES. The system evolves from relatively dense cloud configuration to a sparse coverage (see  
603 Figure 1). The KTF17 parameters do not change significantly during the morphological transition  
604 of the system, which suggests that cycles of cloud growth and decay of cloud patches may be  
605 independent of the large-scale behavior of the system. This result, however, is conditional on the  
606 one LES we considered and it is likely that the KTF17 parameters are indeed sensitive to changes  
607 in other meteorological conditions, e.g., in the boundary conditions. Future work will explore this  
608 idea with a range of LES in different meteorological conditions.

## 609 Acknowledgments

610 We thank Prof. Joceline Lega of the University of Arizona for interesting and inspiring discussion.  
611 GF acknowledges a long collaboration with Ilan Koren on the predator prey model as applied to  
612 cloud systems.

613 SL and MM gratefully acknowledge support by the National Science Foundation under grant DMS-  
614 1619630. FG acknowledges support by a National Research Council Research Associateship award  
615 at the National Oceanic and Atmospheric Administration (NOAA), by the Innovational Research  
616 Incentives Scheme Veni of the Netherlands Organisation for Scientific Research and by The Branco  
617 Weiss Fellowship – Society in Science, administered by the ETH Zurich.

## 618 References

- 619 Agee, E. M. (1984). Observations from space and thermal convection: A historical perspective.  
620 *Bulletin of the American Meteorological Society*, 65(9):938–949.
- 621 Asch, M., Bocquet, M., and Nodet, M. (2017). *Data Assimilation: Methods, Algorithms, and*  
622 *Applications*. SIAM, Philadelphia.
- 623 Boucher, O., Randall, D., Artaxo, P., Bretherton, C., Feingold, G., Forster, P., Kerminen, V.-M.,  
624 Kondo, Y., Liao, H., Lohmann, U., Rasch, P., Satheesh, S., Sherwood, S., Stevens, B., and Zhang,  
625 X. (2013). Clouds and aerosols. In Stocker, T. F., Qin, D., Plattner, G.-K., Tignor, M., Allen, S.,  
626 Boschung, J., Nauels, A., Xia, Y., Bex, V., and Midgley, P., editors, *Climate Change 2013: The*  
627 *Physical Science Basis. Contribution of Working Group I to IPCC AR5: Clouds and Aerosols*.  
628 Cambridge.

- 629 Chorin, A. and Hald, O. (2013). *Stochastic Tools in Mathematics and Science*. Springer, New York,  
630 third edition.
- 631 Christen, J. A., Fox, C., et al. (2010). A general purpose sampling algorithm for continuous distri-  
632 butions (the t-walk). *Bayesian Analysis*, 5(2):263–281.
- 633 Feingold, G. and Koren, I. (2013). A model of coupled oscillators applied to the aerosol cloud  
634 precipitation system. *Nonlinear Processes in Geophysics*, 20(6):1011–1021.
- 635 Feingold, G., Koren, I., Yamaguchi, T., and Kazil, J. (2015). On the reversibility of transitions  
636 between closed and open cellular convection. *Atmospheric Chemistry and Physics*, 15(13):7351–  
637 7367.
- 638 Foreman-Mackey, D., Hogg, D. W., Lang, D., and Goodman, J. (2013). Emcee: the MCMC hammer.  
639 *Publications of the Astronomical Society of the Pacific*, 125(925):306.
- 640 Gilks, W., Richardson, S., and Spiegelhalter, D. (1996). Introducing Markov chain Monte Carlo. In  
641 Gilks, W., Richardson, S., and Spiegelhalter, D., editors, *Markov Chain Monte Carlo in Practice*,  
642 chapter 1, pages 1–20. Springer-Science+Business Media.
- 643 Glassmeier, F. and Feingold, G. (2017). Network approach to patterns in stratocumulus clouds.  
644 *Proceedings of the National Academy of Sciences*, 114(40):10578–10583.
- 645 Goodman, J. and Weare, J. (2010). Ensemble samplers with affine invariance. *Communications in*  
646 *applied mathematics and computational science*, 5(1):65–80.
- 647 Koren, I. and Feingold, G. (2011). Aerosol–cloud–precipitation system as a predator-prey problem.  
648 *Proceedings of the National Academy of Sciences*, 108(30):12227–12232.
- 649 Koren, I. and Feingold, G. (2013). Adaptive behavior of marine cellular clouds. *Scientific Reports*,  
650 3:2507.
- 651 Koren, I., Tziperman, E., and Feingold, G. (2017). Exploring the nonlinear cloud and rain equation.  
652 *Chaos: An Interdisciplinary Journal of Nonlinear Science*, 27(1):013107.
- 653 Maclean, J., Santitissadeekorn, N., and Jones, C. K. (2017). A coherent structure approach for  
654 parameter estimation in Lagrangian data assimilation. *Physica D: Nonlinear Phenomena*, 360:36–  
655 45.
- 656 Morzfeld, M., Adams, J., Lunderman, S., and Orozco, R. (2018). Feature-based data assimilation  
657 in geophysics. *Nonlinear Processes in Geophysics*, 25(2):355–374.
- 658 Myhre, G., Shindell, D., Bréon, F.-M., Collins, W., Fuglestedt, J., Huang, J., Koch, D., Lamarque,  
659 J.-F., Lee, D., Mendoza, B., Nakajima, T., Robock, A., Stephens, G., Takemura, T., and Zhang,  
660 H. (2013). Anthropogenic and natural radiative forcing. In Stocker, T. F., Qin, D., Plattner,  
661 G.-K., Tignor, M., Allen, S., Boschung, J., Nauels, A., Xia, Y., Bex, V., and Midgley, P., editors,  
662 *Climate Change 2013: The Physical Science Basis. Contribution of Working Group I to IPCC*  
663 *AR5: Anthropogenic and Natural Radiative Forcing*. Cambridge.
- 664 Nober, F. J. and Graf, H. F. (2005). A new convective cloud field model based on principles of  
665 self-organization. *Atmospheric Chemistry and Physics*, 5:2749–2759.
- 666 Owen, A. (2013). *Monte Carlo Theory, Methods and Examples*.  
667 <https://statweb.stanford.edu/~owen/mc/>.

- 668 Reich, S. and Cotter, C. (2015). *Probabilistic Forecasting and Bayesian Data Assimilation*. Cam-  
669 bridge University Press, Cambridge.
- 670 Schneider, T., Teixeira, J., Bretherton, C. S., Brient, F., Pressel, K. G., Schär, C., and Siebesma,  
671 A. P. (2017). Climate goals and computing the future of clouds. *Nature Climate Change*, 7(1):3.
- 672 Sokal, A. (1996). Monte Carlo methods in statistical mechanics: Foundations and new algorithms.  
673 In C., D.-M., P., C., and A., F., editors, *Functional Integration*, volume 361. NATO ASI Series  
674 (Series B: Physics).
- 675 Tarantola, A. (2005). *Inverse Problem Theory and Model Parameter Estimation*. SIAM, Philadel-  
676 phia.
- 677 Wolff, U. (2004). Monte Carlo errors with less errors. *Computer Physics Communications*,  
678 156(2):143–153.
- 679 Wood, R. (2012). Stratocumulus clouds. *Monthly Weather Review*, 140(8):2373–2423.
- 680 Wood, R. and Hartmann, D. L. (2006). Spatial variability of liquid water path in marine low cloud:  
681 The importance of mesoscale cellular convection. *Journal of Climate*, 19(9):1748–1764.
- 682 Yamaguchi, T., Feingold, G., and Kazil, J. (2017). Stratocumulus to cumulus transition by drizzle.  
683 *Journal of advances in modeling earth systems*, 9:2333–2349.